# MSEC2022-85638

# THIN-FILM NITRATE SENSOR PERFORMANCE PREDICTION BASED ON IMAGE ANALYSIS AND CREDIBILITY DATA TO ENABLE A CERTIFY AS BUILT FRAMEWORK\*

Xihui Wang, Ajanta Saha, Ye Mi, Ali Shakouri, Muhammad Ashraful Alam, George T.C. Chiu, Jan P. Allebach
Purdue University
West Lafayette, IN, USA

#### **ABSTRACT**

In the modern industrial setting, there is an increasing demand for all types of sensors. The demand for both the quantity and quality of sensors is increasing annually. Our research focuses on thin-film nitrate sensors in particular, and it seeks to provide a robust method to monitor the quality of the sensors while reducing the cost of production.

We are researching an image-based machine learning method to allow for real-time quality assessment of every sensor in the manufacturing pipeline. It opens up the possibility of real-time production parameter adjustments to enhance sensor performance. This technology has the potential to significantly reduce the cost of quality control and improve sensor quality at the same time. Previous research has proven that the texture of the topical layer (ion-selective membrane (ISM) layer) of the sensor directly correlates with the performance of the sensor. Our method seeks to use the correlation so established to train a learning-based system to predict the performance of any given sensor from a still photo of the sensor active region, i.e. the ISM. This will allow for the real-time assessment of every sensor instead of sample testing. Random sample testing is both costly in time and labor, and therefore, it does not account for all of the individual sensors.

Sensor measurement is a crucial portion of the data collection process. To measure the performance of the sensors, the sensors are taken to a specialized lab to be measured for performance. During the measurement process, noise and error are

unavoidable; therefore, we generated credibility data based on the performance data to show the reliability of each sensor performance signal at each sample time.

In this paper, we propose a machine learning based method to predict sensor performance using image features extracted from the non-contact sensor images guided by the credibility data. This will eliminate the need to test every sensor as it is manufactured, which is not practical in a high-speed roll-to-roll setting, thus truely enabling a certify as built framework.

#### **NOMENCLATURE**

SMART Scalable Manufacturing of Aware and Responsive Thin Films

R2R Roll-to-roll

ISM Ion-selective membrane

IoT Internet of Things

PET Polyethylene terephthalate

EOS Electro-Optical System

NI National Instruments

MF Manufacturing factors

WE Working electrode

RE Reference electrode

CF Curve fitting

GT Ground truth

LMA Levenberg-Marquardt algorithm

CLAHE Contrast limited adaptive histogram equalization

LBP Local binary pattern

GP Gaussian pyramid

<sup>\*</sup>RESEARCH SUPPORTED BY THE SMART FILMS CONSORTIUM (HTTPS://WWW.PURDUE.EDU/DISCOVERYPARK/BIRCK/RESEARCH/SMART-FILMS.PHP).

MMNM Min-max normalization method

CV Cross-validation

SVR Support vector regression

RBF Radial basis function

RF Random forest

ATRF Alpha-trimmed random forest

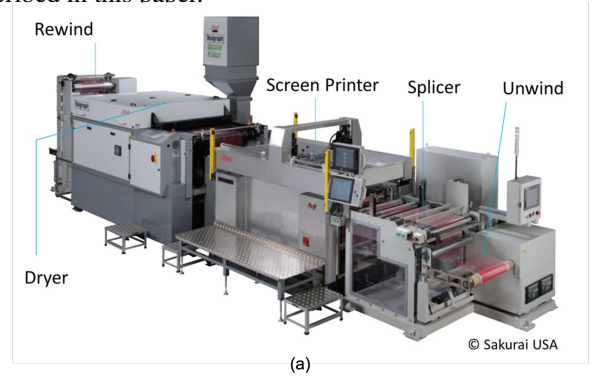
RMSE Root-mean-square error

#### 1 INTRODUCTION

This project is sponsored by the Purdue SMART (Scalable Manufacturing of Aware and Responsive Thin Films) consortium [1], which is comprised of industry leaders and interdisciplinary researchers. The consortium's goal is to develop and produce affordable internet of things (IoT) sensors at commercial volumes and distribute the sensors at a national level. To accomplish this objective, the roll-to-roll (R2R) manufacturing system shown in Figure 1 (a) is used to print the electrodes on a polyethylene terephthalate (PET) substrate, and then coat the electrodes with the ion-selective membrane (ISM) and a silicon passivation layer. Figure 1 (b) shows an example of a fabricated thin-film nitrate sensor batch.

A major challenge of this manufacturing method is efficient and economical quality control. According to the study of nitrate sensors, the sensor performance is influenced by the non-uniform coating of the ISM [2], [3]. These variations in coating thickness will create a visible texture of the sensor surface. Based on this hypothesis, we have been researching and developing a learning-based non-contact imaging approach to predict the performance of a sensor. The experimental results from the past [4], [5], have confirmed the validity of the hypothesis. In this paper, the re-

sults from these previous studies are combined in an integrated manner. Figure 2 shows the modified prediction system structure described in this paper.



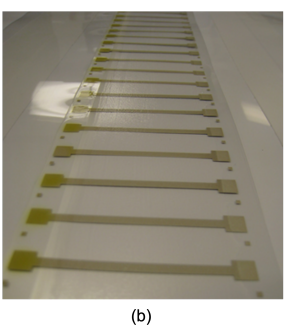


**FIGURE 1**. (a) R2R Sensor Manufacturing System; (b) Example of Fabricated Sensor Batch.

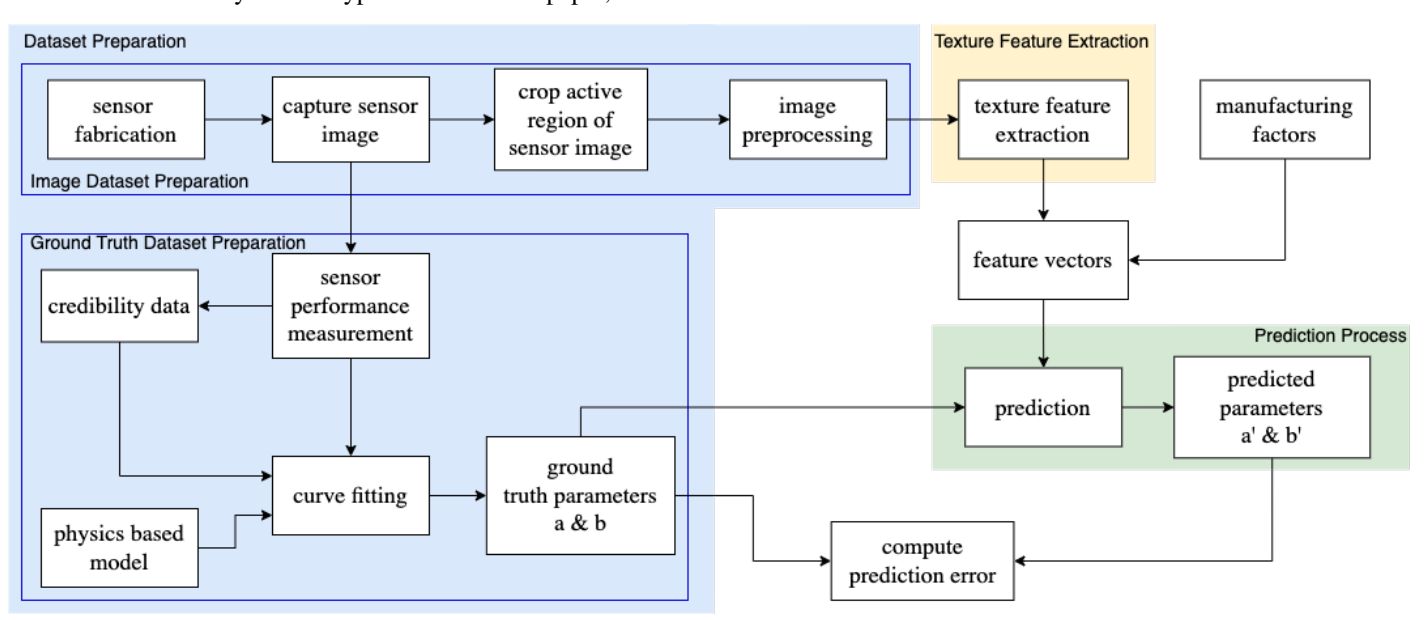


FIGURE 2. Overview of Prediction System for Training and Inferencing.

As with the previous procedure [4], we apply segmentation and texture enhancement techniques to the captured noncontact sensor images to create the image dataset for our prediction model. A logarithmic function derived from the physics model [3] is applied to represent the sensor performance curve, as mentioned in the previous study. The objective of this paper is to use the credibility data to guide this performance data collection process. Details will be discussed in Section 3 (the blue region shown in Figure 2).

Since the texture difference in the nitrate sensor surface is related to the sensor performance, we need to extract meaningful texture features from the sensor image [4]. The feature vector is generated by combining the extracted features and some manufacturing factors as input to the prediction model. In Section 4, we will discuss this in further detail (the yellow region shown in Figure 2).

The normalization process for the input feature vector has been modified for the prediction system part. Other machine learning models were explored to further optimize the prediction accuracy. This will be discussed in greater detail in Section 5 (the green region shown in Figure 2).

# 2 Experiment Setup

# 2.1 Sensor Image Capture Setup

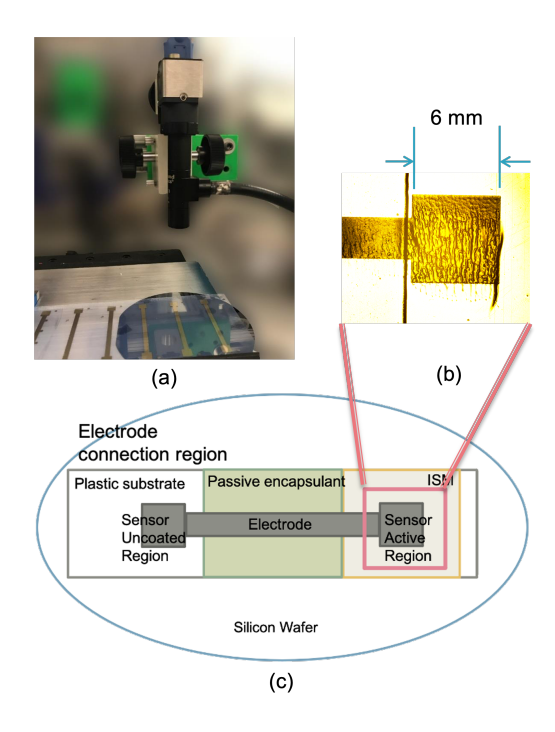


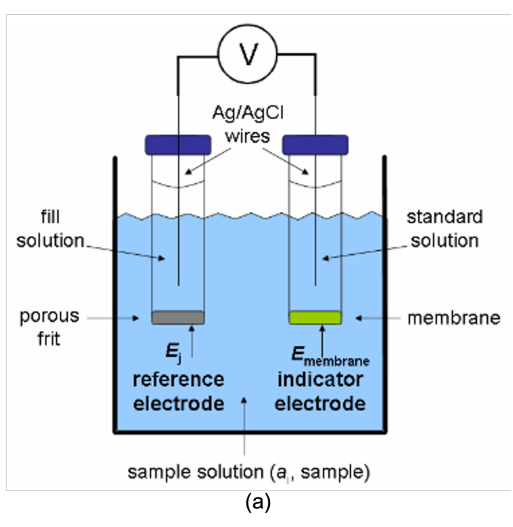
**FIGURE 3**. (a) Experiment Setup for Capturing Sensor Images:

- (b) Example of Captured Sensor Active Region Image;
- (c) Diagram of the Thin-film Nitrate Sensor.

To ensure the consistency of the experiment, the exact equipment setup shown in Figure 3 (a) and procedure are followed as previously [6] to capture the non-contact sensor images in this experiment.

The active region of the nitrate sensor is the electrode coated with the ISM as shown in Figure 3 (c). This is the region that draws the most attention and correlates with sensor performance. An Electro-Optical System (EOS)<sup>1</sup> camera with a microscope is used to capture the active region of the sensor image as demonstrated in Figure 3 (b).

#### 2.2 Sensor Performance Measurement Setup



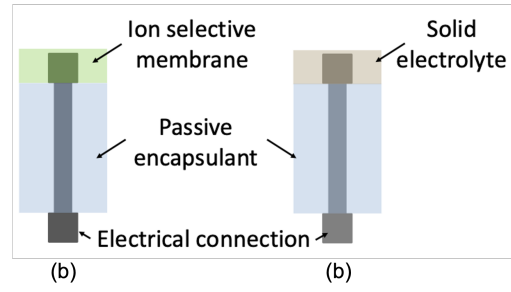


**FIGURE 4**. (a) Sensor Voltage Measurement Experiment Setup;

- (b) Structure of Indicator Electrode;
- (c) Structure of Reference Electrode.

During the sensor performance measurement procedure, the active region of the working electrode (also known as indicator electrode shown in Figure 4 (b)) will be soaked in the nitrate solution, while the non-coated electrode connection region will be

<sup>&</sup>lt;sup>1</sup>Electro-Optical System Inc, Phoenixville, PA 19460.

connected to the National Instruments (NI) Module<sup>2</sup> to record the potential voltage data as shown in Figure 4 (a). Meanwhile, the reference electrode (shown in Figure 4 (c)) with the solid electrolyte coating is connected to the NI Module in the same way to provide a stable reference electrochemical potential signal. The sensor performance signal of the working electrode is the difference in voltage between the two [7].

### 3 Dataset Preparation

### 3.1 Image Data Preparation

The non-uniform ISM coating causes the texture difference displayed in the captured sensor active region image and affects the sensor performance. A segmentation method is implemented so that the prediction model only focuses on the pattern of the active region shown in the top row of Figure 5. A preprocessing step is added to the overall prediction system to enhance the texture details of the sensor active region image as shown in the bottom row of Figure 5.

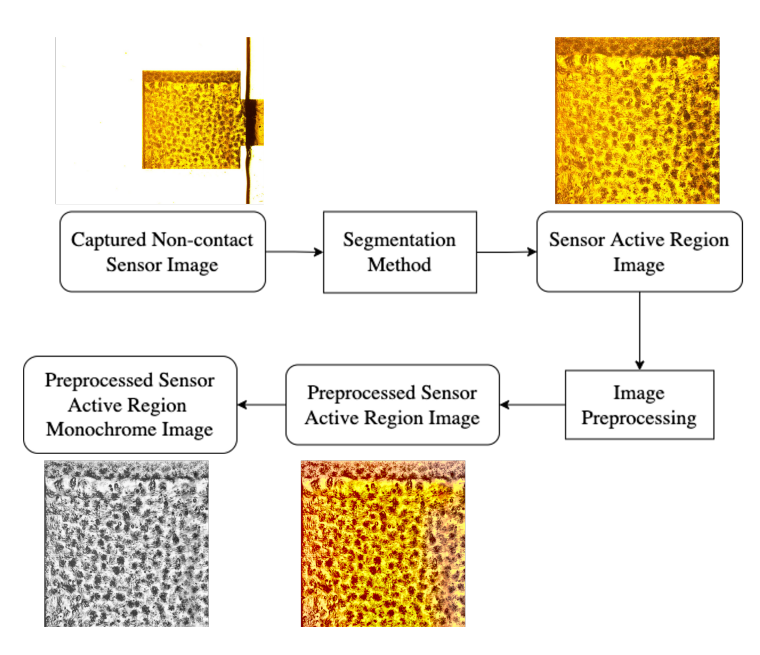


**FIGURE 5**. Image Data Preparation Procedure.

To segment the sensor active region image, we are using the template matching technique [8]. The preprocessing step is mainly based on the contrast limited adaptive histogram equalization (CLAHE) method [9] applied to the lightness channel. Due to the fact that the texture extraction methods (will discuss in Section 4) are applied to grayscale images, we select the lightness channel based on the previous experiments. A description of

the implementation details is provided in the previous work [4].

### 3.2 Sensor Performance Data Preparation

The sensor potentiometric responses used in this experiment are measured by the setup shown in Figure 4 (a) for around 22 hours using 0.001 molar nitrate solutions. The sensor potential signals will achieve their saturated phase after about 4.5 hours. Outlier sensor response signals caused by measurement error need to be eliminated before generating the ground truth parameters. The modified curve fitting method is then applied to the sensor saturated region suggested by the physics-based model for all the inlier sensor responses. The generated ground truth parameters will represent the entire measured performance signal and will be fed into the prediction model.

#### 3.2.1 Dynamic Credibility Data Generation

In the ground truth dataset, we want to exclude the faulty sensors so that they do not affect our training process. If a sensor becomes defective due to imperfect manufacturing or electrical measurement, the potential response of the sensor will deviate from the rest of the sensors in the group. In that case, we assign low credibility to the sensor. We calculate credibility using the Bayesian Maximum Likelihood Estimation (MLE) approach [10]. In this approach, we give the continuous time potential response of a group of sensors as input. We first calibrate the potential response of all sensors to bring them to the same level since reliable sensors can show constant bias due to manufacturing or measurement variability. We then divide the full-time series data into short time periods and assign a credibility score to each sensor at each time period based on the MLE approach. MLE gives high credibility to a sensor that frequently agrees with the majority of that period for a given time period. We use overlapping time windows to keep the memory of the previous time window. Thus, MLE gives a dynamically evolving credibility score of each sensor for the whole time frame.

The dynamic credibility data plays a significant role in both procedures, the outlier exclusion procedure and ground truth parameter generation procedure. The dynamic credibility data is calculated by comparing the shape of each performance signal among all the performance signals in the same manufacturing run based on a Bayesian model [10]. We denote the raw sensor performance signal as  $V_m$ , then the dynamic credibility data is calculated from  $V_m$  with a window size equal to 20 data points, and overlap of 5 data points [11]. Thus for a given sensor, we obtain a credibility value at each time-point.

# 3.2.2 Outlier Exclusion

The outliers in this experiment are caused by human error during the measurement of sensor performance rather than sensor defects.

<sup>&</sup>lt;sup>2</sup>NI (formerly National Instruments), Austin, TX 78759-3504)

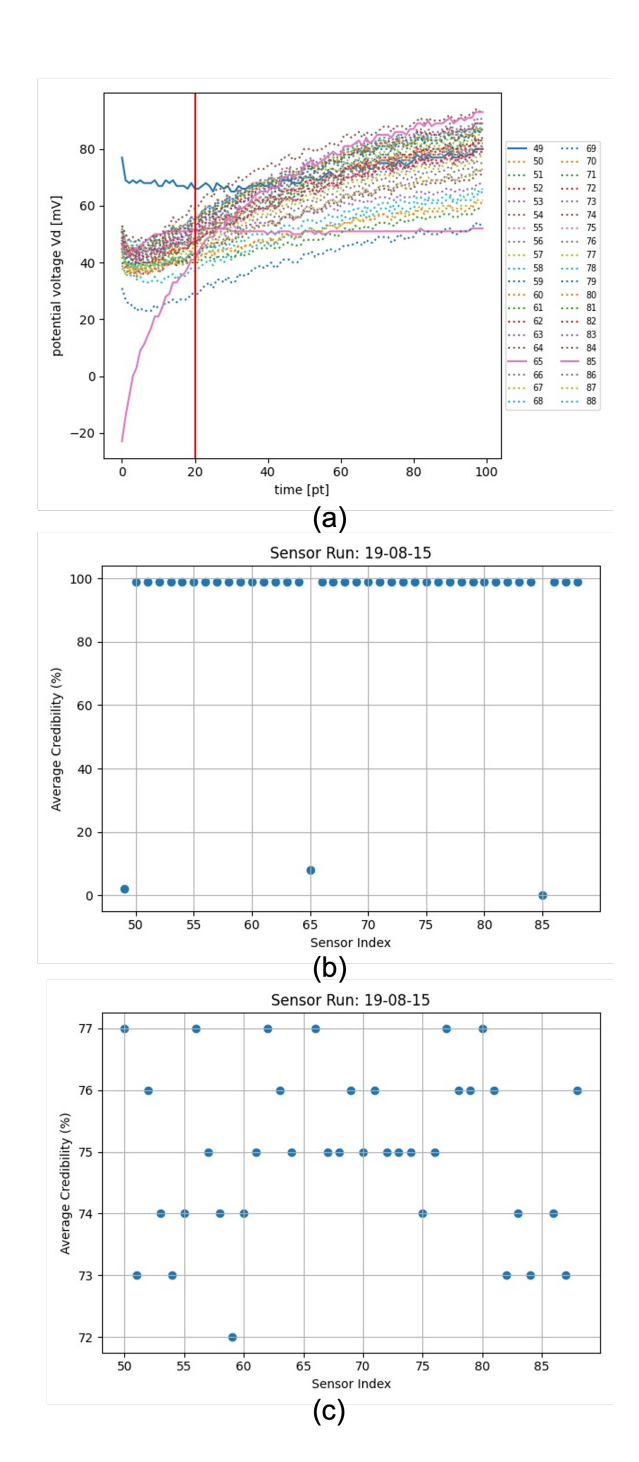


**FIGURE 6**. Outlier Exclusion Example.

- (a) Raw Sensor Performance Data;
- (b) Average Credibility Data for Entire Sensor Run;
- (c) Average Credibility Data for Inliers.

To eliminate the outliers, a binary threshold is set at 70% for the average credibility data. The dynamic credibility data is then calculated again after eliminating the outliers that fail to meet the threshold criterion. We repeat this process until the average credibility data is above 70% for all the remaining sensors, indicating that only inliers are left. The dynamic credibility data, denoted as c, will be used to guide the curve fitting process for each inlier sensor later.

Figure 6 provides an example of excluding the outliers from an example sensor run. Figure 6 (a) provides the original measured sensor performance signal where the solid lines represent the outlier signals caused by measurement error. The x-axis represents time and the y-axis represents the potential voltage in mV. Figure 6 (b) shows the average credibility data of each sensor calculated with all the sensors. The x-axis represents sensor index, and the y-axis represents the average credibility data in percentage. Figure 6 (c) shows the average credibility data of the inlier sensors. The axes are same as Figure 6 (b). Notice that the vertical scales of Figures 6 (b) and (c) are different since the credibility data are calculated based on different sensor groups.

# 3.2.3 Curve Fitting Process for Inliers

The modified curve fitting process simplifies the sensor performance curve into the ground truth parameters for all the inlier sensor performance signals, as shown in Figure 7. A 5th order Savitzky-Golay smoothing filter [12] with window length equal to 100 data points is applied on the raw measured data, the same as before [4].

The physics-based model [3] suggests that the change of potential voltage over time is a logarithmic growth. Hence, the following equation is used here to generate the ground truth parameters a and b.

$$V_{fit}(t) = a \cdot log(t) + b \tag{1}$$

The weighted Levenberg-Marquardt algorithm [13], [14] is used to find the ground truth parameter combination  $\beta=(a,b)$  that gives the best fitting logarithmic curve  $V_{fit}(t,\beta)$  for the saturated region of  $V_s$ . The relationship between the weighting factor  $\sigma$  and the dynamic credibility data c is  $\sigma=\frac{1}{c}$ . Here,  $V_s$  denotes the downsampled and smoothed sensor performance signal.

$$\hat{\beta} = \arg\min_{\beta} \sum_{i=1}^{N} \left( \frac{V_s(i) - V_{fit}(i, \beta)}{\sigma_i} \right)^2 \tag{2}$$

$$= \arg\min_{\beta} \sum_{i=1}^{N} [c_i(V_s(i) - V_{fit}(i, \beta))]^2$$
 (3)

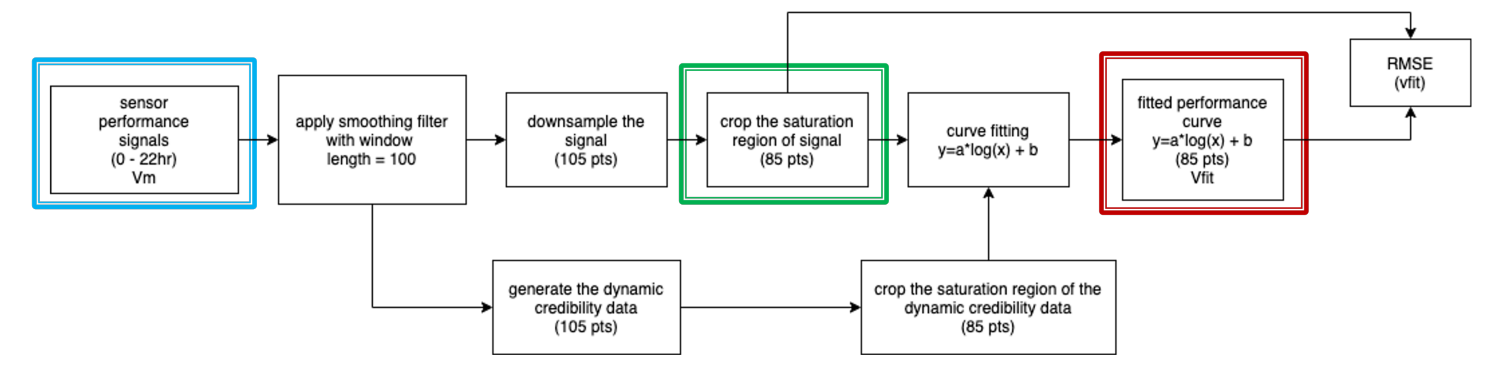


FIGURE 7. Ground Truth Data Preparation Procedure Applied to the Inlier Sensor Data after Outlier Exclusion Based on the Credibility Analysis.

The accuracy of the fitted curve is evaluated by the weighted root-mean-square error (RMSE) (denoted as  $RMSE_{CF}$ ), where CF stands for the curve fitting process and N is the total number of time points.

$$RMSE_{CF}(mV) = \sqrt{\frac{1}{N} \sum_{i=1}^{N} c_i \left( V_{fit}(i) - V_s(i) \right)^2}$$
 (4)

Figure 8 (a) illustrates the difference between the downsampled original measured sensor performance signal  $V_m$ , the downsampled and smoothed signal  $V_s$ , and the fitted curve  $V_{fit}$  in the saturated region. The  $RMSE_{Vm}$  is the weighted RMSE calculated between  $V_{fit}$  and the downsampled  $V_m$  while the  $RMSE_{Vs}$  is the weighted RMSE calculated between  $V_{fit}$  and the downsampled smoothed  $V_s$ . Figure 8 (b) shows the dynamic credibility c for the corresponding sensor.

The dataset generated for this experiment contains 108 sensors. The average  $RMSE_{CF}$  for the curve fitting process is around 0.5566 mV between  $V_{fit}$  and the downsampled smoothed data  $V_d$ , and 0.9915 mV between  $V_{fit}$  and the downsampled raw data  $V_m$ . The result indicates that the idea of using the ground truth parameters  $\beta$  to represent the saturated region of the sensor's potentiometric response is reliable.

#### 4 Texture Feature Extraction

The visual texture differences of the sensor active region caused by the non-uniform ISM coating is related to the sensor performance. Hence, extracting meaningful texture features from the collected sensor image data is critical to predicting sensor performance accurately. Two types of local binary pattern (LBP) descriptors [15] and the Gaussian pyramid (GP) method [16] were discussed in the previous experiments [4], and they will be used again in the following experiment.

In the study of pattern classification in computer vision, the LBP texture operator is one of the most common operators. The

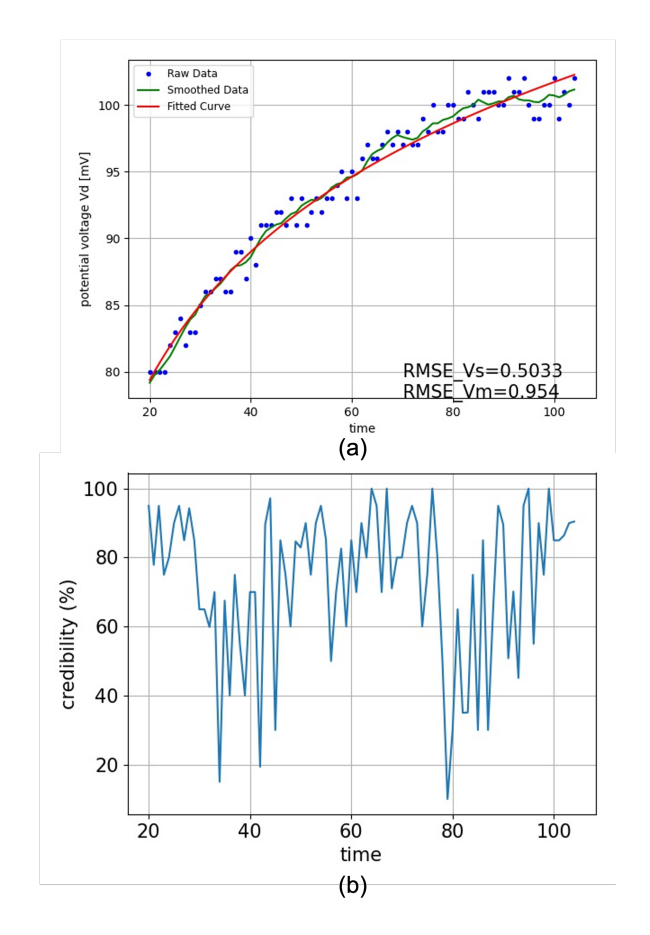


**FIGURE 8**. (a) Example of Fitted Logarithmic Curve; (b) Dynamic Credibility Data.

LBP operator encodes the texture pattern of each pixel in the grayscale image based on the predefined small neighborhood region to an LBP number. Figure 9 shows an example of applying an LBP descriptor on the given sensor image. The x-axis of the LBP histogram is the LBP number. The y-axis of the LBP his-

togram is the percentage among all the pixels of that LBP value. Each highlighted LBP number shown in the LBP histogram represents the highlighted region in the given sensor image.

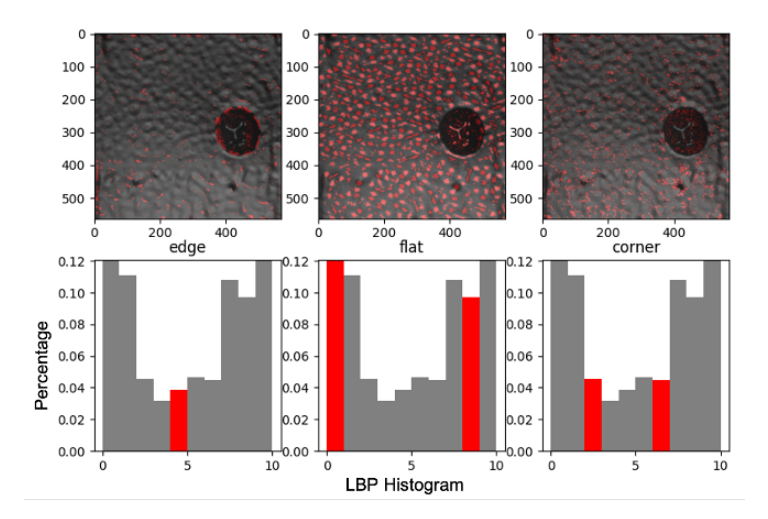


**FIGURE 9**. Example of LBP Patterns and LBP Histograms.

The GP method is a multiscale image processing technique based on applying a Gaussian filter on the image and then downsampling the image so that the resolution for each layer will be 1/4 of that of the previous layer. The number of GP layers in this experiment was set to three (as seen in Figure 10)

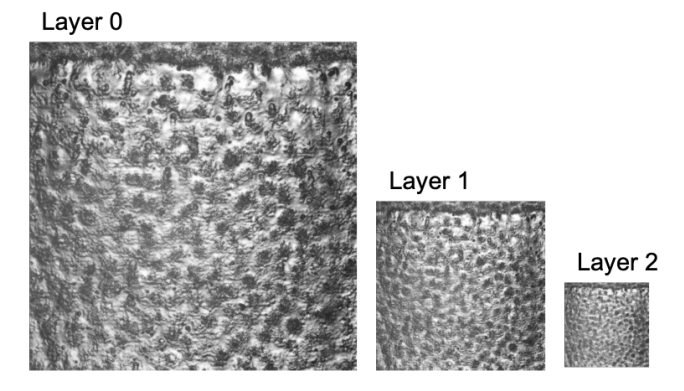
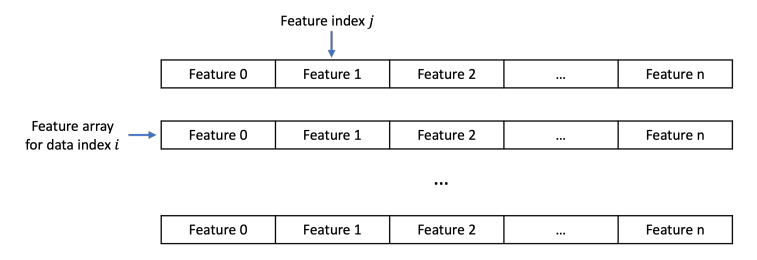


FIGURE 10. Example of Gaussian Pyramid.

The feature vector used by the prediction model is constructed by combining the manufacturing factors and the texture features extracted from the preprocessed sensor active region images. The manufacturing factors include the average measured sensor thickness data and three R2R sensor manufacturing setting parameters: solid content, line speed, and flow rate.

As the features are in various ranges, data normalization is necessary before feeding the feature vectors to our prediction model. Here, we use the min-max normalization method (MMNM) to normalize each feature to range [0, 1], as shown in Equation (5). We denote i as the data sample index, j as the feature index,  $x_{i,j}$  as the j-th feature of the i-th data, and  $x_{i,j}$  as the normalized  $x_{i,j}$ . The structure of the feature vector for each sample data is shown in Figure 11.

$$\hat{x_{i,j}} = \frac{x_{i,j} - min(x_j)}{max(x_i) - min(x_j)}$$
(5)



**FIGURE 11**. Structure of Feature Vectors for Each Data Sample.

#### 5 Prediction Models

The structure of the expanded image-based prediction system is shown in Figure 12.

Relative to what we reported in [4], we have modified the feature vector normalization process and changed the prediction model to a multi-output regression model [17] with two types of regressors. Multi-output regression is a strategy that allows one to run several regressors in parallel.

Because of the two target variables a and b (the ground truth parameters), a multi-output regression model combined with other regressors is considered in the prediction system. This strategy consists of fitting one regressor per target variable and running them in parallel.

Let us denote the fitted curve generated based on the ground truth parameters a and b as  $V_{fit}$  and the predicted curve calculated based on the predicted parameters a' and b' as  $V_{pred}$ .

$$V_{fit}(t) = a \cdot log(t) + b \tag{6}$$

$$V_{pred}(t) = a' \cdot log(t) + b' \tag{7}$$

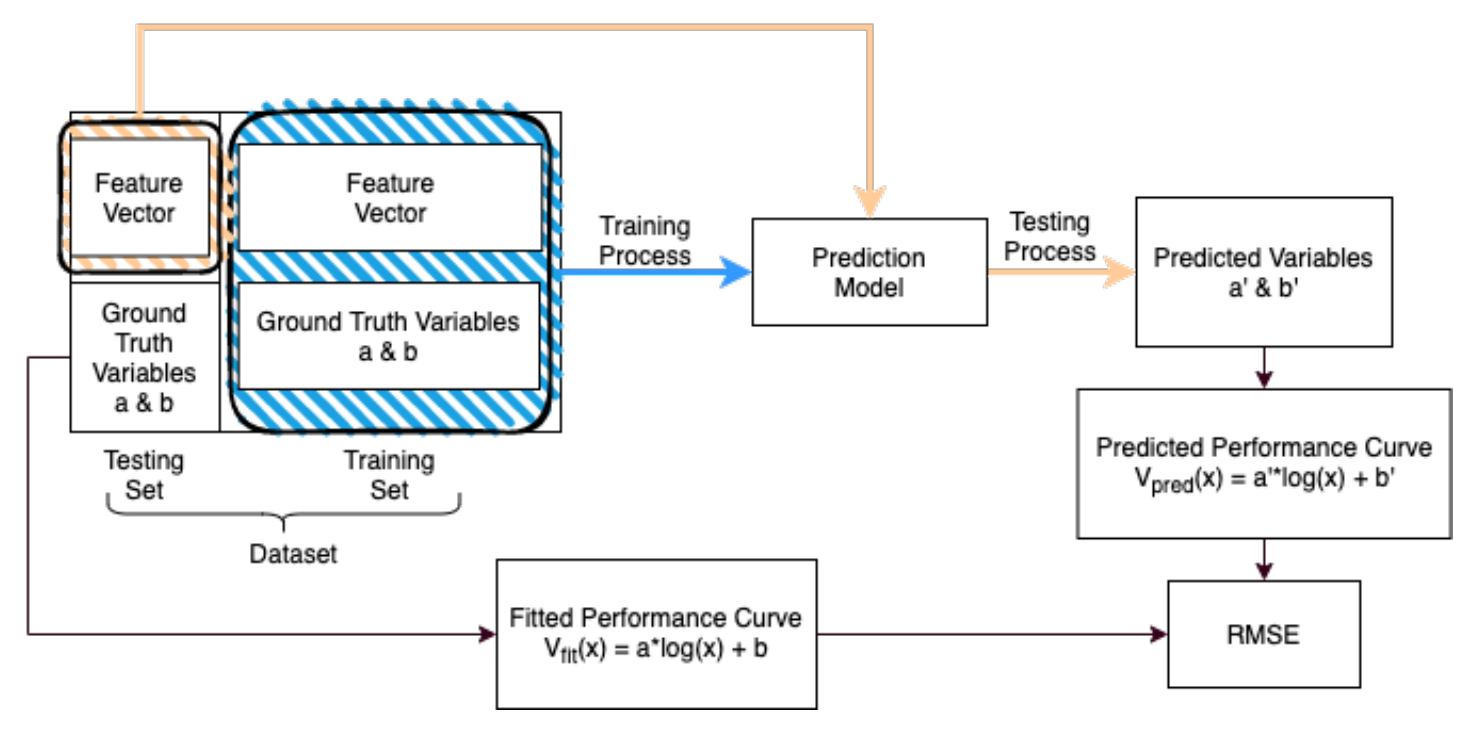


FIGURE 12. Structure of The Prediction Model.

The root-mean-square error (RMSE) is used to evaluate the prediction performance of the prediction system.  $RMSE_{pred}$  calculates the error between the predicted curve  $V_{pred}$  and the fitted curve  $V_{fit}$ .

$$RSME_{pred} = \sqrt{\frac{1}{N} \sum_{i} (V_{pred}(i) - V_{fit}(i))^2}$$
 (8)

# 5.1 Support Vector Regression (SVR)

The SVR model has been used in our previous research [4], [5] as it is the most commonly used machine learning model for the regression problem. The SVR model [18] deals with the regression problem by finding an appropriate hyperplane that fits the input data in higher dimensions under the proper hyperparameter setting. The radial basis function (RBF) kernel [19] is used in our SVR model because of the non-linear relationship between the feature vector and the performance parameters.

# 5.2 Alpha-trimmed Random Forest (ATRF)

The alpha-trimmed random forest (ATRF) method is constructed from the random forest (RF) method.

The random forest (RF) method [20] is an ensemble learning method that constructs a number of decision trees and uses the bagging technique [21] simultaneously to ensure randomness

during training. Samples are randomly chosen from the whole training dataset with replacement to form unique training subsets based on the concept of the bagging technique. Each decision tree is then trained by the given subset, and the trees running in parallel build a random forest. The predicted value of the RF is the average of the predicted values from the trees.

The alpha-trimmed random forest (ATRF) method is executed by applying the concept of the alpha-trimmed mean filter [22] to the predicted values from the decision trees inside the forest to obtain the predicted value of the ATRF. The concept of the alpha-trimmed filter is to deduct the percentage  $\alpha/2$  of the smallest and largest values from the group and output the average value of the remaining variables in the group as demonstrated in Figure 13 [23]. 20% of the total predicted variables in the forest are trimmed in this experiment. The structure of the ATRF is shown in Figure 14.

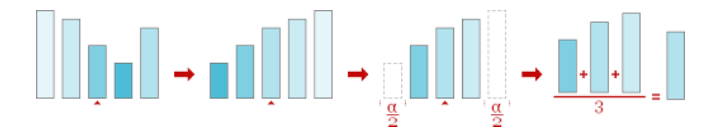
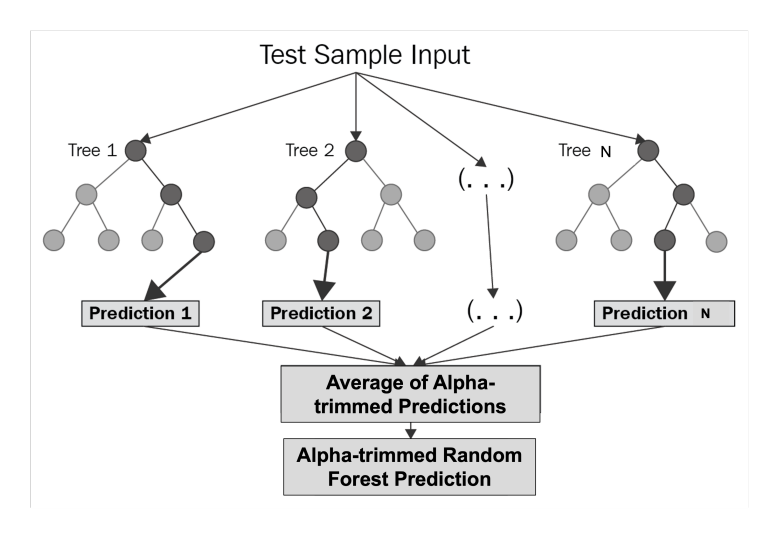


FIGURE 13. Example of Alpha-trimmed Mean Filter Calculation.



**FIGURE 14**. Alpha-trimmed Random Forest Structure.

### 6 Experimental Results

The dataset used in this experiment contains 108 sensors from four different manufacturing runs indicated by different colors shown in Figure 15.

As shown in Figure 15, sensors from different manufacturing runs show various performance behaviors. From the physics hypothesis model, we learned that this variation is caused by the non-uniform ISM coating on the sensor active region during the manufacturing process. Rows 1-3 in Figure 16 (solid content, line speed, flow rate) are the setting parameters during the sensor fabrication process for each sensor manufacturing run. Row 4 is the measured average thickness of the sensor in each sensor run. The columns are the manufacturing factors for the four different sensor manufacturing runs. Row 5 provides two sensors

sor active region images for each sensor run. Row 6 provides the monochrome images generated from the images in Row 5. From Figure 16 and Figure 15, we could notice that the sensor surface texture, the sensor performance signal, and the manufacturing factors for each sensor run are all different. Therefore using dataset containing the four sensor runs can prove the generalization of our prediction system in some sense.

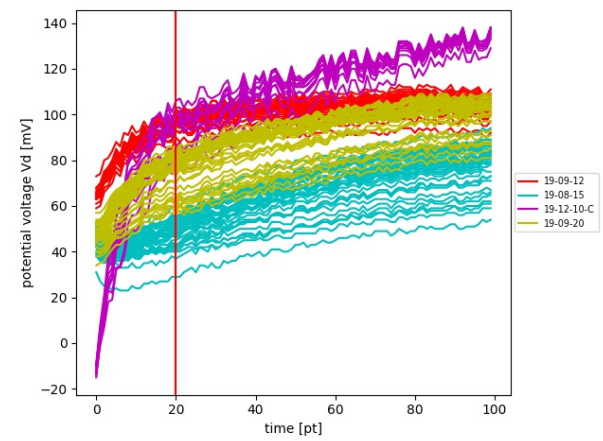


**FIGURE 15**. Sensor Performance Signals from Four Sensor Manufacuring Runs.

The image dataset and the ground truth dataset are collected as discussed in Section 3. The 5-fold cross-validation method is applied during the training and evaluation procedure of the image-based prediction system. The overall system performance is represented by the average predicted performance among all folds.

		Sensor Run (Date of Coating)	2019-08-15	2019-09-12	2019-09-20	2019-12-10_C
Manufacturing Factors (MF)	1	Coating solution solids (wt. %)	22.3	22.3	22.3	26.1
	2	Line speed (m/min)	0.25	0.15	0.2	0.15
	3	Flow rate (mL/min)	0.6	0.36	0.48	0.6
	4	Thickness (micron)	11.8	10.4	14.4	23.7
	5	Active region image examples of each sensor run	on mage			
	6	Preprocessed active region image examples of each sensor run	en e			

FIGURE 16. Difference Between Sensor Manufacturing Runs.

**TABLE 1**. Feature Vectors Implemented in the Image-based Prediction System

Method	Feature Vector	# of Features
M1	LBP(uniform) + MF	14
M2	LBP(nri_uniform) + MF	62
M3	GP + LBP(uniform) + MF	34
M4	GP + LBP(nri_uniform) + MF	178

The feature vectors with which we have experimented are listed in Table 1. Each feature in each method will be normalized to the range  $[0,\,1]$  using Equation (5) and then fed into the prediction system. As discussed previously [4], the uniform and nri\_uniform LBP descriptors are under the same setting: P=8 pixels and R=3 pixels. The Gaussian pyramid (GP) contains three layers, and MF represents the settings for the manufacturing factors during the sensor fabrication process.

The RMSE (calculated with Equation (8)) is used to evaluate the accuracy of the predicted sensor performance for each fold. The average RMSE and the standard deviation of the RMSE in each fold are used to estimate the performance of the image-based prediction system. The accuracy and the robustness of the image-based prediction system are shown in Table 2 for the SVR model and in Table 3 for the ATRF model.

**TABLE 2**. Prediction Results for SVR Model

Method	RMSE(mV)	StDev(mV)	
M1	5.9094	1.1194	
M2	6.7825	1.3033	
M3	6.2308	1.1690	
M4	6.5245	1.0633	

**TABLE 3**. Prediction Results for ATRF Model

Method	RMSE(mV)	StDev(mV)	
M1	6.0726	1.0214	
M2	6.1380	1.0258	
M3	6.1213	1.0362	
M4	6.5588	1.1077	

#### 7 Conclusion

Our image-based prediction system is designed to accurately predict the potentiometric responses of thin-film nitrate sensors given their preprocessed active region images.

The two models perform similarly in terms of accuracy. However, the SVR model achieves a better prediction performance, which is 5.9094 mV, while the standard deviation for the AMRF model is somewhat lower than that of the SVR model.

Compared to what we reported previously [4], in this paper, a novel way of generating the ground truth parameters for inlier sensors using the dynamic credibility data is proposed in the dataset preparation section. The average credibility data is calculated repeatedly to exclude the outlier sensors. The weighted Levenberg-Marquardt algorithm helps us to generate more accurate ground truth parameters guided by the dynamic credibility data. The prediction model is modified using the multi-output regression model. The AMRF method is implemented as an additional machine learning model. With these advances, we can achieve a robust system that can support high-volume manufacturing of low-cost thin film nitrate sensors.

#### **REFERENCES**

- [1] SMART Films Consortium. Birck Nanotechnology Center, Purdue University, West Lafayette, IN. URL https://engineering.purdue.edu/SMART.
- [2] Hu, J., Stein, A., and Bühlmann, P., 2016. "Rational design of all-solid-state ion-selective electrodes and reference electrodes". *TrAC Trends in Analytical Chemistry*, 76, pp. 102–114.
- [3] Jin, X., Saha, A., Jiang, H., Oduncu, M. R., Yang, Q., Sedaghat, S., Maize, K., Allebach, J. P., Shakouri, A., and Glassmaker, N. J., 2021. "Steady-state and transient performance of ion-sensitive electrodes suitable for wearable and implantable electro-chemical sensing". *IEEE Transactions* on *Biomedical Engineering*.
- [4] Wang, X., Maize, K., Mi, Y., Shakouri, A., Chiu, G. T. C., and Allebach, J. P., 2021. "Thin-film nitrate sensor performance prediction based on preprocessed sensor images". *Electronic Imaging*, **2021**(16), pp. 341–1.
- [5] Yang, Q., Maize, K., Jin, X., Jiang, H., Alam, M. A., Rahimi, R., Chiu, G. T. C., Shakouri, A., and Allebach, J. P., 2020. "Predicting response of printed potentiometric nitrate sensors using image based machine learning". NIP & Digital Fabrication Conference, pp. 108–113.
- [6] Yan, Y., Yang, Q., Maize, K., Allebach, J. P., Shakouri, A., and Chiu, G. T. C., 2019. "Image-based non-contact conductivity prediction for inkjet printed electrodes". NIP & Digital Fabrication Conference, pp. 152–157.
- [7] Sedaghat, S., Jeong, S., Zareei, A., Peana, S., Glassmaker, N., and Rahimi, R., 2019. "Development of a nickel oxide/oxyhydroxide-modified printed carbon electrode as

- an all solid-state sensor for potentiometric phosphate detection". *New Journal of Chemistry*, **43**(47), pp. 18619–18628.
- [8] Brunelli, R., 2009. *Template matching techniques in computer vision: theory and practice.* John Wiley & Sons.
- [9] Reza, A. M., 2004. "Realization of the contrast limited adaptive histogram equalization (CLAHE) for real-time image enhancement". *Journal of VLSI Signal Processing Systems for Signal, Image and Video Technology,* 38(1), pp. 35–44.
- [10] Meng, C., Jiang, W., Li, Y., Gao, J., Su, L., Ding, H., and Cheng, Y., 2015. "Truth discovery on crowd sensing of correlated entities". In Proceedings of the 13th ACM conference on embedded networked sensor systems, pp. 169–182.
- [11] Saha, A., and Alam, M. A. "Reliable sensing with wearable and implantable sensors in the wild environment (in processing)".
- [12] Savitzky, A., and Golay, M. J. E., 1964. "Smoothing and differentiation of data by simplified least squares procedures". *Analytical Chemistry*, 36(8), pp. 1627–1639.
- [13] Gavin, H. P., 2019. "The Levenberg-Marquardt algorithm for nonlinear least squares curve-fitting problems". *Department of Civil and Environmental Engineering, Duke University*, pp. 1–19.
- [14] Moré, J. J., 1978. *The Levenberg-Marquardt algorithm:* implementation and theory. Springer.
- [15] Ojala, T., Pietikäinen, M., and Harwood, D., 1996. "A comparative study of texture measures with classification based on featured distributions". *Pattern Recognition*, **29**(1), pp. 51–59.
- [16] Adelson, E. H., Anderson, C. H., Bergen, J. R., Burt, P. J., and Ogden, J. M., 1984. "Pyramid methods in image processing". *RCA Engineer*, *29*(6), pp. 33–41.
- [17] Multi-output regressor. URL https://scikit-learn.org/stable/modules/generated/sklearn.multioutput.
  MultiOutputRegressor.html.
- [18] Smola, A. J., and Schölkopf, B., 2004. "A tutorial on support vector regression". *Statistics and Computing*, *14*(3), pp. 199–222.
- [19] Musavi, M. T., Ahmed, W., Chan, K. H., Faris, K. B., and Hummels, D. M., 1992. "On the training of radial basis function classifiers". *Neural Networks*, *5*(4), pp. 595–603.
- [20] Biau, G., and Scornet, E., 2016. "A random forest guided tour". *Test*, *25*(2), pp. 197–227.
- [21] Breiman, L., 1996. "Bagging predictors". *Machine Learning*, *24*(2), pp. 123–140.
- [22] Bednar, J., and Watt, T., 1984. "Alpha-trimmed means and their relationship to median filters". *IEEE Transactions on Acoustics, Speech, and Signal Processing*, **32**(1), pp. 145–153.
- [23] Chernenko, S. Alpha-trimmed mean filter. URL